2026 IEEE International Conference on Robotics and Automation (ICRA 2026)
June 1-5, 2026. Vienna, Austria

Force Estimation and Position Control of a Hydraulic Folded Pouch Actuator for Soft Robotics

Jie Li, Jianlin Yang, Jinling Qiu, Hanqi Lou, Zhangxi Zhou and George Mylonas

Abstract— **This paper investigates position control and force estimation for a hydraulic folded pouch actuator. First, experimental platforms are designed to characterize the actuator and the results show two key properties: (i) angular hysteresis when the motion direction reverses, and (ii) strong nonlinearity between liquid volume, pressure, and angle. For position control, we explore three strategies: fully open-loop control, observer-based control, and sensor-based closed-loop control with angle feedback. The closed-loop controller employs dynamically tuned PID gains and an MLP feedforward predictor. Under a sinusoidal reference, the closed-loop controller achieves mean absolute error (MAE) = 4.82° and root mean square error (RMSE) = 5.48°. For force estimation, we train both MLP and LSTM models using liquid volume, angle, pressure, and angular rate as features to predict the external force on the actuator. Compared to the MLP, the LSTM incorporates temporal dynamics, which allows it to capture force variations more effectively and generate smoother prediction results. Under dynamic loads, both models capture the applied force, with the LSTM yielding the lower errors (MAE = 0.96 mN·m, RMSE = 1.23 mN·m).**

I. INTRODUCTION

Soft robotics has emerged as a rapidly developing field that offers unique advantages over traditional rigid robotic systems. By leveraging compliance, lightweight structures, and intrinsic adaptability, soft robots can safely interact with humans, conform to complex environments, and perform delicate manipulation tasks that would be challenging for rigid robots [1].

Among the various components of a soft robotic system, actuators play a central role, as they directly determine the robot's motion capability, adaptability, and interaction performance. One of the most classical soft actuators is the contraction-type pneumatic artificial muscle, whose mechanical behavior closely resembles that of biological muscles. Typical examples include the McKibben pneumatic artificial muscle [2] and pouch motors [3]. These actuators can generate relatively large forces and exhibit muscle-like contraction, making them attractive for bio-inspired robotics and wearable assistive devices. However, their widespread application has been hindered by a limited stroke (with a maximum contraction ratio of about 36% theoretically), which restricts their motion range and versatility. A variety of strategies have been proposed to address this drawback, such as chain-link design [4], origamic chamber design [5], gusseted pouch motor [6], and paired pouch motor [7] to increase both displacement and output force. While these approaches can partially increase the stroke, they typically achieve no more than 50% contraction ratio, and often at the cost of more complex structures and fabrication processes.

In recent years, folded-type artificial muscles have gained attention due to their extremely simple structure and capability of achieving ultra-large strokes and considerable force output while maintaining low fabrication cost and compactness [8]–[13]. Some of them have been applied for soft wearable devices to assist joint movement [9]–[11], while some of them are used for actuating soft surgical robots [12], [13]. However, most existing studies on folded actuators remain focused on structural design, and proof-of-concept demonstrations in robotic systems. Their accurate control is restricted by the highly nonlinear deformation. Model-based strategies, such as model predictive control (MPC), require an explicit system model to predict future states and optimize control inputs. However, accurately deriving dynamic models and identifying model parameters for soft actuators is challenging due to material hysteresis, complex pressure variations, and continuously changing geometries [14]. Moreover, while most folded actuators are fluid-driven, which exhibit intrinsic sensing potential, the highly complex variations in fluid pressure in folded actuators make force perception particularly challenging. Consequently, there is an urgent need to develop effective strategies that can enable precise position control and reliable force perception in folded actuators.

To address this gap, this paper presents a study on the position control and force estimation of a hydraulic folded pouch actuator using neural network-based methods. Leveraging the nonlinear approximation capability of neural networks, the actuator is able to achieve not only stable force estimation but also robust trajectory tracking under varying load conditions. By adopting a data-driven framework, the proposed approach removes the requirement for explicit modeling of complex control and force-estimation, thereby simplifying system implementation while preserving practical effectiveness.

II. ACTUATOR CHARACTERISTICS

A. Design of Folded Pouch Actuator

Fig.1(a)-(c) shows the working principle of a folded pouch actuator. The pouch is deflated and folded without fluid. When filled with fluid, the folded pouch actuator unfolds until fully straightened to provide motion and force. The actuator pouch is fabricated from a solvent-bonded PE/PET/PE triple-laminate film (30/12/35 μm), consisting of polyethylene (PE) and polyethylene terephthalate (PET),

Jie Li, Jianlin Yang, Jinling Qiu, Hanqi Lou, Zhangxi Zhou and George Mylonas are with the Hamlyn Centre, Institute of Global Health Innovation, Imperial College London, London, W2 1PF, U.K. (e-mail: jianlin.yang@imperial.ac.uk).

Jie Li and Jianlin Yang contributed equally to this work. (Corresponding author: Jianlin Yang.)

which ensures biocompatibility. The folded pouch was manufactured using a laser welding machine, as described in [15]. The welding trajectory is illustrated by the black lines in Fig.1(d). The pouch is cut along the predefined path using a laser cutter (FLUX BEAMO, Europe), shown as the red lines. Fig.1(e) and (f) shows its deflated and inflated states. The chamber size is 40 mm×15 mm when deflated.

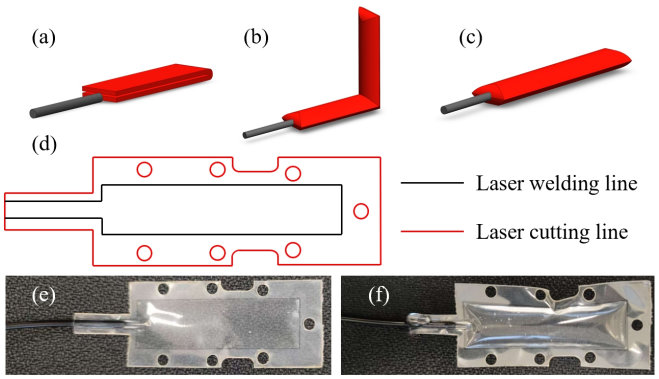

Fig. 1: Pouch actuator description. (a)-(c) Working principle of pouch actuator. (d) Actuator manufacturing. (e) Deflated state. (f) Inflated state.

B. Actuator Test Platform

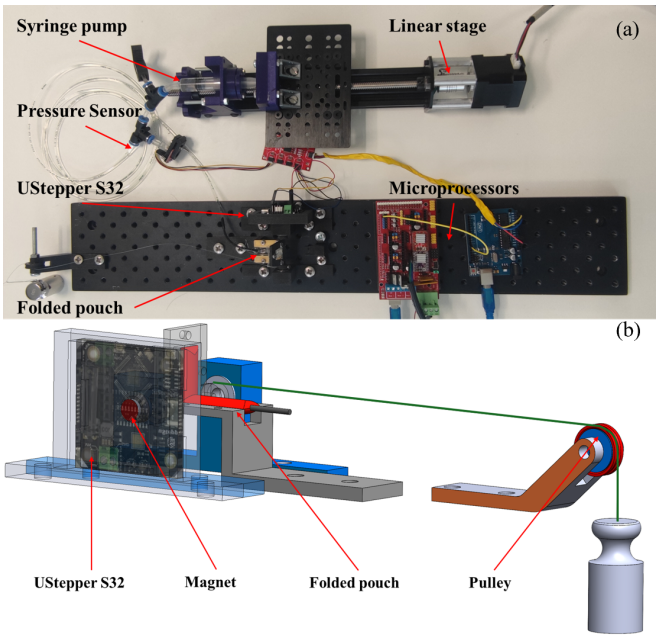

Fig. 2: The test platform for the actuator characteristics. (a) Platform setup. (b) Principle of platform.

Fig.2(a) illustrates the experimental platform used to characterize the folded pouch actuator. The actuator is hydraulically driven by a syringe pump, which is connected via a 1m-long tube with an outer diameter of 3 mm. A pressure sensor (SparkFun MS5803-14BA) is employed to monitor the internal liquid pressure, while the Hall sensor integrated in the uStepper S32 (uStepper ApS, Denmark), with an angular resolution of 0.011°, is used to measure the angular displacement of the folded pouch. A constant load is applied using calibrated weights. An Arduino Mega is responsible for collecting all sensor data, and a RAMPS1.4 board is used to control the stepper motor on a NEMA17 ACME lead screw linear actuator (OOZNEST, UK), which drives the syringe pump to deliver water into the actuator. As shown in Fig.2(b), one side of the actuator is fixed, while the other side is mounted on a rotatable plate using screws. A magnet is mounted on the shaft of the rotating plate, aligned with the center of the uStepper S32 Hall sensor for angle measurement. The constant load provided by the attached weights enables the folded pouch to fold, while the Hall sensor continuously records the angular displacement of the pouch during its rotational motion.

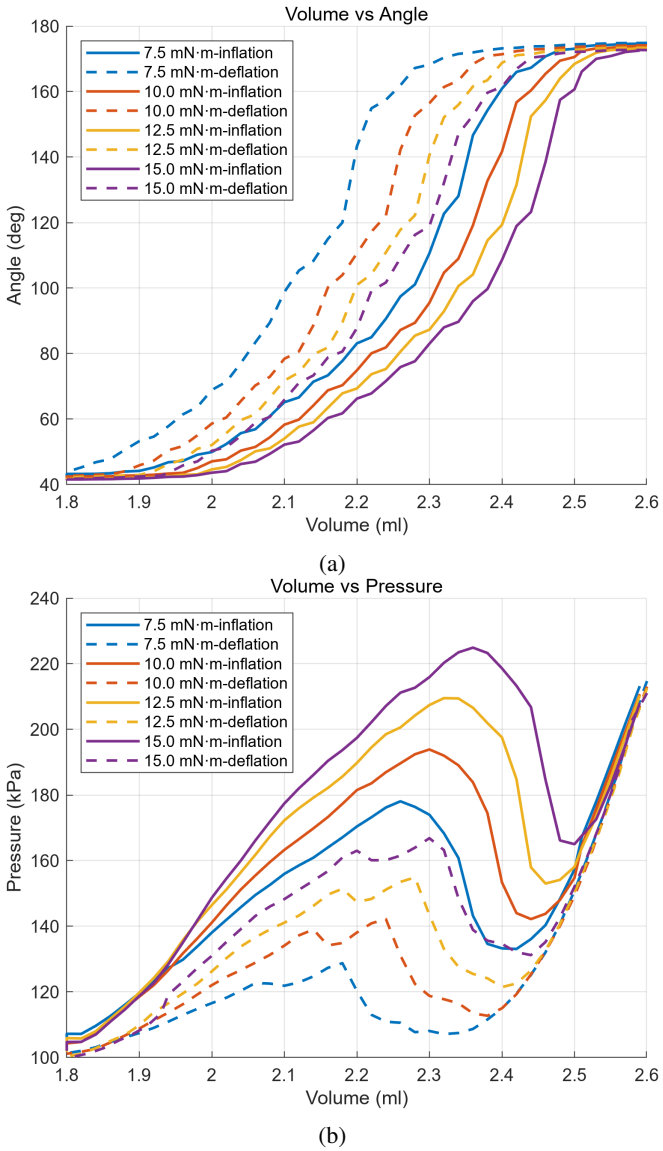

Fig. 3: Characteristics of folded pouch actuator. (a) Angle displacement versus liquid volume under different payloads. (b) Pressure versus liquid volume under different payloads.

Fig.3 presents the characterization results of the pouch actuator. The maximum liquid volume that can be injected into the pouch is 2.6 mL, with the operational range from 1.8 to 2.6 mL. Within this range, the folding angle varies between 50° and 180°. To characterize the actuator, constant torques were applied using weights ranging from 150 g to 300 g. The torque was calculated as the product of the weight and the radius of the cylindrical rod (5 mm). Torque ranges from 7.5 mN·m to 15.0 mN·m. Fig.3(a) illustrates the relationship between input liquid volume and angular displacement under different torques, where solid lines represent the inflation process and dashed lines represent the deflation process. As shown in Fig.3(a), the actuator exhibits a nonlinear hysteresis behavior: during the deflation process, angular displacement lags behind that of the inflation process. Fig.3(b) shows the corresponding pressure variations, highlighting the strong nonlinearities of the system. Notably, in the volume range of approximately 2.3–2.6 mL, the pressure curve exhibits a local decrease followed by a subsequent increase. This phenomenon is attributed to the structural transition of the folded pouch. As the actuator progresses from a folded configuration toward a fully unfolded state, the effective cross-sectional area at the folding crease increases abruptly. This sudden geometric expansion reduces the internal fluid pressure temporarily. Once the pouch continues to expand beyond this transition, the pressure rises again with further volume injection. These results indicate that it is difficult to model the relationships between volume, angle, and pressure of the pouch actuator.

To capture the relationship between liquid volume, internal pressure, and torque of the folded pouch actuator under dynamic and randomly varying loads, an experimental platform (Fig.4) was designed to collect the datasets. The setup combines a load cell (resolution: 50 mN, SparkFun Qwiic Scale NAU7802) and pulley system to apply varying external torques to the folded pouch actuator, while simultaneously measuring the tensile load transmitted to the actuator. This configuration enables synchronized acquisition of actuator states under time-varying load conditions, including liquid volume, internal pressure, angular displacement, and the corresponding applied force. In total, the dataset consists of approximately 5400 samples, encompassing a wide range of loading scenarios. These include constant loads, monotonically increasing loads, monotonically decreasing loads, and randomly varying loads.

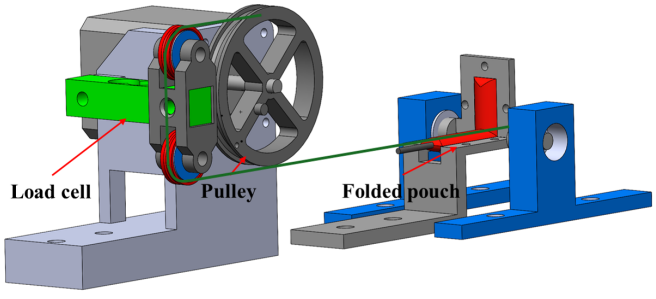

Fig. 4: Platform to collect actuator data under varying load.

III. Position Control of the Actuator

A. Control Performance Evaluation

To evaluate the proposed control strategies, three controllers—open-loop, observer-based control, and closed-loop control—were tested under identical experimental conditions. A sinusoidal reference signal with amplitude ranging from 90° to 150° and a period of 20 s was used as the desired trajectory. Each experiment was conducted over five consecutive cycles to assess the performance of controllers. All tests were performed on the constant load platform described in Fig.2 and Fig.4. Four different payloads were applied using calibrated weights of 150 g, 200 g, 250 g, and 300 g (torques ranging from 7.5 mN·m to 15 mN·m) to validate the performance under varying payloads.

The performance of the proposed control models is assessed with evaluation metrics including the coefficient of determination mean absolute error (MAE), root mean squared error (RMSE) and maximum error.

B. Open-Loop Control

The open-loop control of the pouch actuator is implemented based on the fitted relationships between liquid volume and angular displacement under different payloads, as shown in Fig.3(a). Fifth-order polynomial models were employed to approximate the nonlinear mapping between liquid volume and angular displacement. Because of the hysteresis observed during the deflation process, two separate polynomial curves were used to represent the inflation and deflation phases, respectively. Given the payload, the controller selects the calibration polynomial for that load condition. The workflow of open-loop position control is shown in Fig.5.

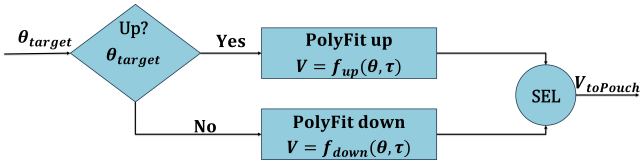

Fig. 5: The open-loop position control system.

Fig.6 shows the results of the open-loop control experiment. Due to stress relaxation in the soft material, the actual angular displacement gradually decreases as the number of cycles increases during sine-wave tracking. In addition, when the external load is increased, the overall angular displacement curve shifts downward. Since two separate polynomial curves are employed to represent the inflation and deflation processes for each torque value, a noticeable angular fluctuation occurs at the transition points where the direction of motion changes.

C. Observer-based control

A learning-based method was applied to estimate the angular displacement of folded pouch actuator. The overall control system with angle estimation observer is shown in Fig.7. To capture the nonlinearity and hysteresis relationship

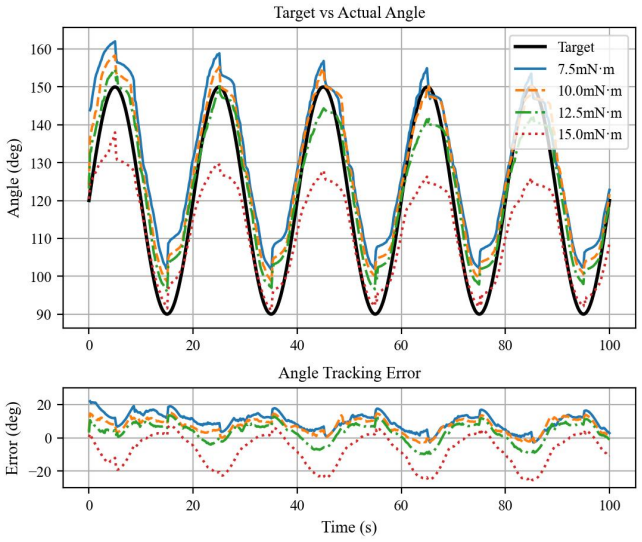

Fig. 6: The open-loop control results.

between input liquid volume, internal pressure and load, a multilayer perceptron (MLP) [16] regressor was trained on the dataset collected with the platform shown in Fig.4. For this task, the input features are the instantaneous liquid volume V (mL), internal pressure P (kPa), applied load τ (mN·m), and a finite-difference angle increment $\Delta\theta$ (defined as the difference between two consecutive measured angular positions) encoding motion direction and hysteresis. The model outputs the estimated angle $\hat{\theta}_{est}$:

$$\hat{\theta}_{est}(k) = f_\theta\big(V(k),\, P(k),\, \tau(k),\, \Delta\theta(k)\big), \tag{1}$$

where f_θ denotes the trained MLP model and k represents the discrete time step index.

To improve response speed and reduce lag caused by hysteresis, a feedforward inverse model is introduced. Using the same MLP framework, this model maps from the desired angle, current pressure, and load to the volume command required to reach the target:

$$\hat{V}_{\text{ff}} = f_\phi\big(\theta_{\text{des}},\, P,\, \tau\big). \tag{2}$$

During operation, the feedforward term provides an initial input to the syringe pump, while the residual error

$$e(k) = \theta_{\text{des}}(k) - \hat{\theta}_{\text{est}}(k), \tag{3}$$

is corrected by a dynamically tuned PID controller. The PID gains were first tuned under two extreme loads, 150 g (7.5 mN·m) and 300 g (15 mN·m), yielding parameter sets $\{K_p^{\min}, K_i^{\min}, K_d^{\min}\}$ and $\{K_p^{\max}, K_i^{\max}, K_d^{\max}\}$. During operation, the controller interpolates between them based on the instantaneous error $e(k)$:

$$K_j(e) = \alpha(e)\, K_j^{\max} + \big(1 - \alpha(e)\big)\, K_j^{\min}, \quad j \in \{p, i, d\},$$

where $\alpha(e) \in [0, 1]$ is a monotonic function of $|e(k)|$. A typical formulation is

$$\alpha(e) = \frac{|e(k)|}{|e(k)| + c}, \quad c > 0, \tag{4}$$

such that $\alpha(e) \to 0$ as $|e(k)| \to 0$ and $\alpha(e) \to 1$ as $|e(k)| \to \infty$.

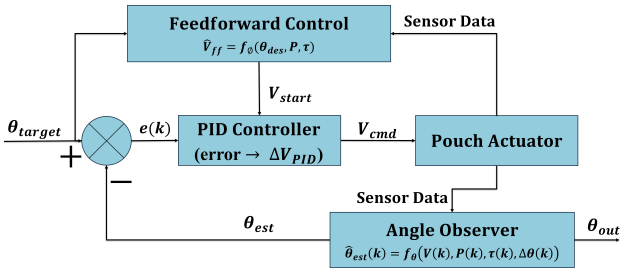

Fig. 7: Observer-based control system.

Fig.8 shows the results of observer-based control. Overall, across different payloads, the angle prediction system is able to utilize the feedback of internal pressure and injected volume to estimate the actuator's angular displacement and track the prescribed sine trajectory. However, due to stress relaxation of the soft material, the amplitude gradually decreases as the number of cycles increases. This relaxation changes the internal pressure of the pouch for the same load and angular displacement. In addition, the amplitude decreases with increasing the external load. Furthermore, when the motion direction changes from inflation to deflation, a noticeable prediction lag is observed, which leads to a delayed overall trajectory tracking response.

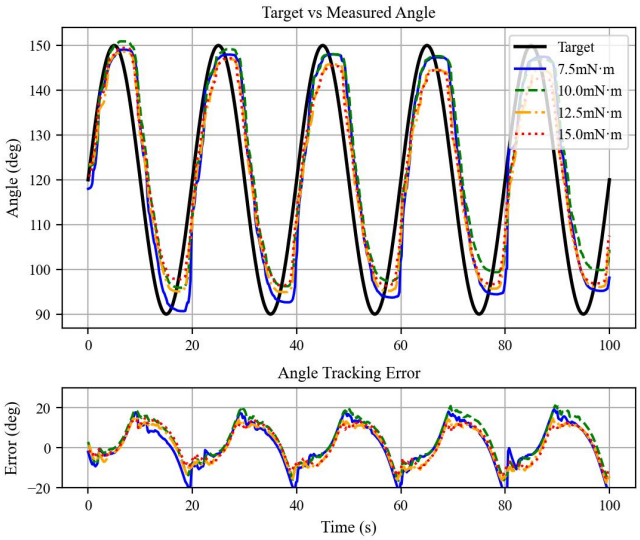

Fig. 8: The observer-based control results.

D. Closed-Loop Control

In this section, we implemented closed-loop control using the Hall sensor to measure the actuator's angle. The closed-loop structure, shown in Fig.9, employs the same dynamic PID scheme, combined with the feedforward MLP model described above.

Fig.10(a) shows the results of closed-loop control. Overall, the closed-loop controller enables the folded pouch actuator to accurately follow the prescribed sine trajectory. Under

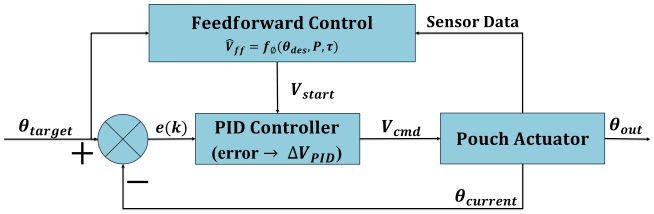

Fig. 9: The closed-loop control system.

different payloads, the tracking curves converge to a similar profile, demonstrating that the controller maintains fast and stable performance under different load conditions. Due to the inherent hysteresis of the folded pouch actuator, the dominant tracking errors are observed primarily during direction reversals, where the actuator exhibits delayed responses to changes in motion direction. Fig.10(b) indicates the tracking results under dynamic load, while the changing load is provided by the platform shown in Fig.4. The results further prove the robustness of the controller.

Table I summarizes the quantitative tracking performance of the three control strategies over five tracking cycles, reported as the average errors across all tested payloads. The open-loop controller achieves basic trajectory tracking but suffers from large errors (MAE = 8.66°, RMSE = 9.55°), particularly under load variation and during motion reversals, due to stress relaxation effects. Incorporating the MLP-based angle estimation improves the performance (MAE = 8.47°, RMSE = 8.70°), as the predictor applies pressure and volume feedback to better capture the actuator's nonlinear response. Compared with the open-loop control, this approach also achieves better consistency of tracking curves across different payloads. However, during the deflation phase, the MLP exhibits estimation inaccuracies, which introduce a temporal lag and lead to increased tracking errors. In contrast, the closed-loop controller significantly enhances accuracy (MAE = 4.82°, RMSE = 5.48° at constant load and MAE = 5.31°, RMSE = 5.95° at dynamic load) and robustness across different loads, with the maximum error reduced to 10.11°. This demonstrates that the folded pouch actuator, despite its inherent nonlinearities in position and pressure, can achieve stable and reliable control with machine learning models and sensor-based feedback.

TABLE I: Tracking performance of different control strategies

	Open-Loop	Angle Estimation	Closed-Loop	Dynamic Load
MAE [°]	8.66	8.47	4.82	5.31
RMSE [°]	9.55	8.70	5.48	5.95
Max Error [°]	25.36	17.42	10.11	11.89

IV. Learning-Based Force Estimation Models

Force sensing capability is crucial for robotic systems, as it enables safer and more precise interactions. However, due to the small, compact, and compliant structure of the pouch

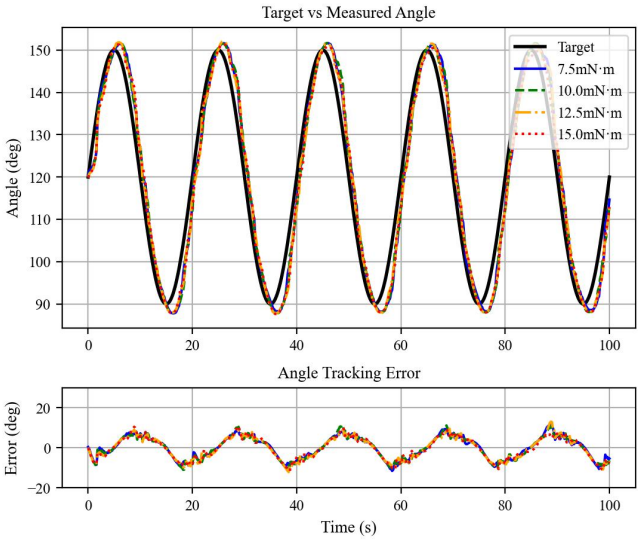

(a)

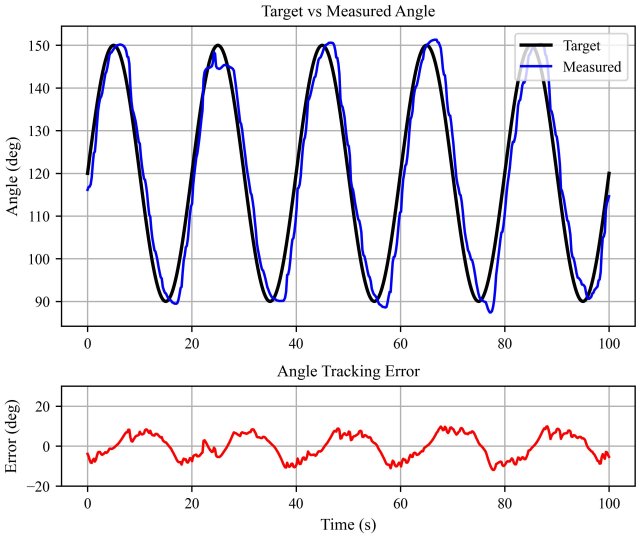

(b)

Fig. 10: The closed-loop control results. (a) Under constant load. (b) Under dynamic load.

actuator, obtaining reliable tactile information is challenging. In addition, this difficulty is further compounded by irregular deformations and the nonlinear relationships between internal fluid volume, pressure, and generated force.

It has been demonstrated that the external load on a fluid-driven actuator can be inferred based on its internal pressure [17]. In this section, we leverage the proximal liquid pressure and employ a neural network-based method to estimate the external load acting on the folded pouch actuator.

A. MLP Force Estimation Model

A data-driven approach was adopted, reusing the unified framework of Section III. In this setting, the MLP is trained to predict the applied force $\hat{F}$ from actuator states:

$$\hat{F}(k) = f_{\psi}\big(V(k),\, P(k),\, \theta(k),\, \Delta\theta(k)\big), \tag{5}$$

where f_ψ denotes the trained force model. Input features mirror those used for position tasks, with the ground-truth torque recorded by the platform shown in Fig.4. The trained MLP captures the dominant nonlinear dependencies, enabling force estimation without direct force sensors.

B. LSTM Force Estimation Model

While the MLP provides a static nonlinear mapping between actuator states and external force, it does not incorporate history-dependent effects such as stress relaxation. In practice, when the folded pouch actuator is subjected to sustained loading, both internal pressure and deformation evolve gradually, and these dynamics vanish once the load is released. These temporal dependencies motivate the adoption of a recurrent sequence model, specifically a long short-term memory (LSTM) [18] network, to effectively capture history-dependent behaviors.

Let the instantaneous actuator state be

$$\mathbf{x}(k) = \big[V(k),\, P(k),\, \theta(k), \Delta\theta(k)\big]^\top, \tag{6}$$

where V is liquid volume, P is pressure, and θ is angular displacement. Instead of mapping $\mathbf{x}(k)$ directly to force, the LSTM processes a sliding window of past states

$$\mathbf{X}_{k-w+1:k} = \big(\mathbf{x}(k-w+1), \ldots, \mathbf{x}(k)\big), \tag{7}$$

and outputs the predicted force

$$\hat{F}(k) = f_\omega^{\mathrm{LSTM}}\big(\mathbf{X}_{k-w+1:k}\big), \tag{8}$$

where f_ω^{LSTM} denotes the recurrent network parameterized by ω. In our implementation, $w = 5$ is used, with a two-layer LSTM (128 hidden units each) followed by a fully connected readout. The network is trained with mean squared error loss and Adam optimization.

C. Force Estimation Experiments

To evaluate the performance of the proposed force estimation methods, we conducted experiments under both constant-load and dynamic-load conditions. For the constant-load tests, the setup shown in Fig.2 was used, where calibrated weights of 200 g, 250 g, and 300 g were applied, corresponding to torques ranging from 10 mN·m to 15 mN·m. For the dynamic-load tests, the platform in Fig.4 was employed, where a stepper motor was used to rotate the pulley and apply dynamic loads to the folded pouch actuator.

During the evaluation of the force estimation models, the pouch actuator was simultaneously controlled using the closed-loop controller illustrated in Fig.9 and tracked a sinusoidal reference trajectory as shown in Fig.10. While the actuator followed the trajectory, sensor feedback was collected in real time and used by both the MLP- and LSTM-based force estimation models to generate instant predictions of the applied load. The results of both testing conditions are shown in Fig.11 and Fig.12, which compare the estimated forces with the ground-truth under constant and dynamic loading conditions. The error table of force estimation results is summarized in Table II.

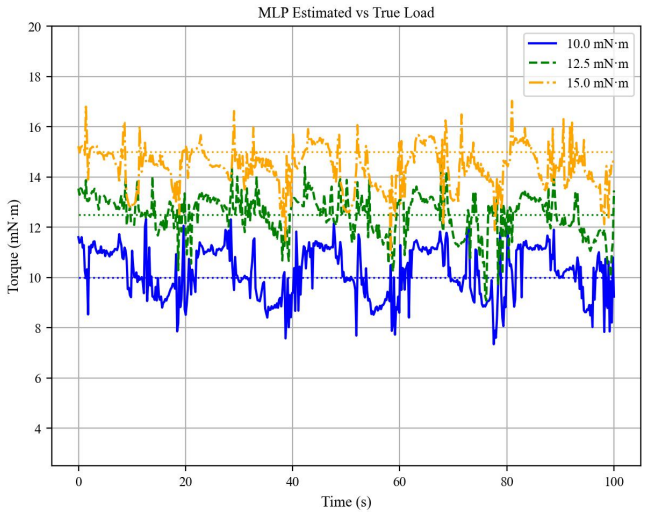

(a)

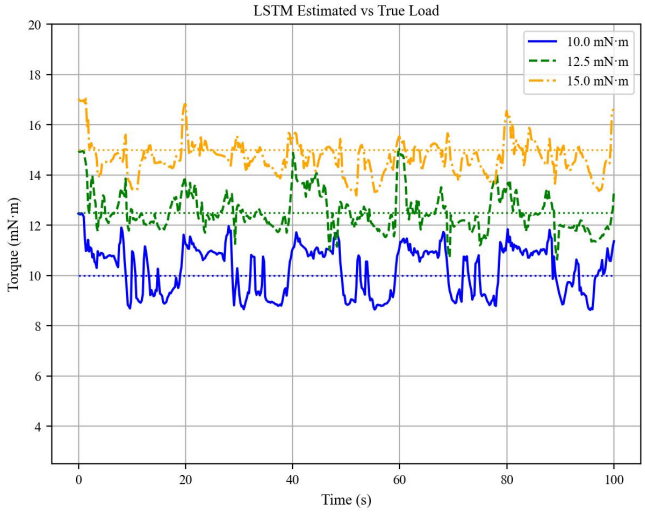

(b)

Fig. 11: Force estimation tracking results of MLP and LSTM under constant Load. (a) MLP tracking results. (b) LSTM tracking results.

TABLE II: Force estimation errors under different loads

Load (g / mN·m)	Model	MAE (mN·m)	RMSE (mN·m)	Max (mN·m)
200 / 10.0	**MLP**	0.90	1.05	2.66
	LSTM	0.90	0.98	2.47
250 / 12.5	**MLP**	0.64	0.81	3.42
	LSTM	0.58	0.78	2.53
300 / 15.0	**MLP**	0.81	1.05	4.12
	LSTM	0.56	0.74	2.04

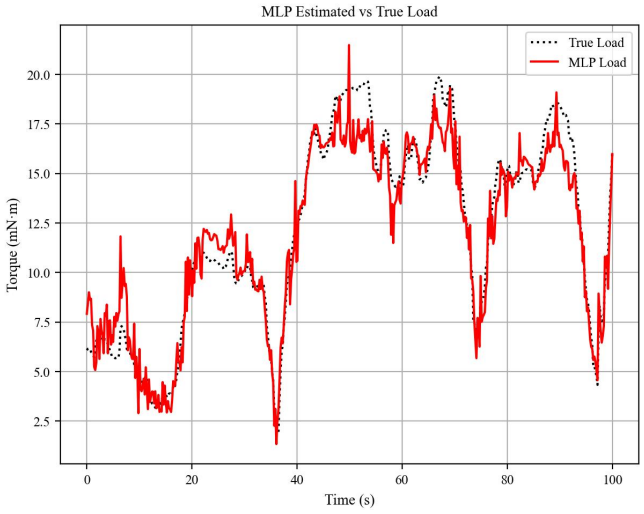

(a)

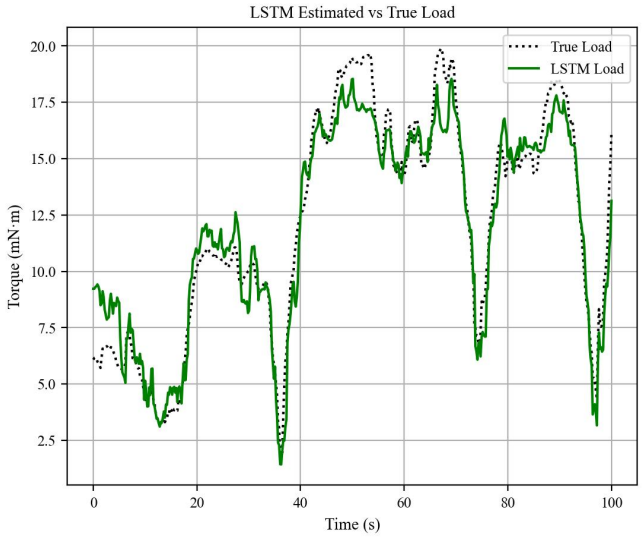

(b)

Fig. 12: Force estimation tracking results of MLP and LSTM under dynamic load. (a) MLP tracking results. (b) LSTM tracking results.

From the overall results of force estimation, both the MLP and LSTM models can effectively distinguish different load conditions under constant and dynamic tests. The MLP estimation exhibits oscillations around the ground-truth curves, while the LSTM outputs are noticeably smoother. This difference arises because the models use the finite-difference angle $\Delta\theta$ as a feature: in the MLP case, noise in this derivative term propagates directly into the estimation, whereas the temporal memory of the LSTM attenuates such fluctuations by exploiting sequential correlations across time.

As summarized in Table II, the LSTM model achieves consistently lower MAE, RMSE, and maximum error compared with the MLP baseline. These results highlight that incorporating temporal dynamics provides advantages in capturing time-varying behaviors, enabling more robust force estimation when the folded pouch actuator operates under dynamic load conditions.

Table III summarizes the performance of different machine learning models for force estimation under dynamic load while tracking sine trajectories. Among these methods, the MLP achieves a good balance between accuracy and inference efficiency. However, the LSTM configuration with hidden size 128 and two layers provides the lowest errors while maintaining competitive inference speed, highlighting the benefit of incorporating temporal dynamics into the estimation framework.

TABLE III: Comparison of force estimation validation results with different models

Model	MAE (mN·m)	RMSE (mN·m)	Max (mN·m)	Inference (ms/sample)
MLP	0.99	1.27	4.64	0.0092
Random Forest	1.20	1.62	6.10	0.0185
SVR	1.35	1.68	6.25	0.3162
XGBoost	1.05	1.45	6.10	0.0042
LSTM (128, 2)	0.96	1.23	3.51	0.0101

V. Conclusion

This paper presented a hydraulic folded pouch actuator and a learning-based framework for position control and force estimation. We first characterized the actuator's static behavior under different torques and documented its pronounced nonlinearity and hysteresis in the volume–angle–pressure relationship. Building on these observations, we developed three control strategies—open-loop, observer-based control, and closed-loop control—and validated them on sinusoidal trajectories and multiple loads. Despite its nonlinear and hysteretic characteristics, the results show that the actuator achieves reliable tracking: the MLP-based angle observer with a feedforward inverse model and a dynamically tuned PID can improve control performance compared to the open-loop model, while direct closed-loop control with Hall-sensor feedback yielded the best accuracy and robustness across loads.

For force perception, it is shown that data-driven models can map readily measured states to the external load without explicit analytical modeling. The MLP provided a compact and deployable baseline, and the LSTM further improved accuracy by capturing relaxation-driven, history-dependent effects. Across constant and dynamic loading scenarios, both models effectively distinguished different load levels, with the LSTM offering smoother predictions and lower errors. A key limitation is the reliance of force estimation on accurate angle feedback. Without direct angle input as a model feature, the external load applied to the pouch actuator cannot be captured. To facilitate the integration of this approach into soft robotic systems, future work will explore non-intrusive angle feedback strategies, including vision-based sensing [19], electrical impedance [20] and liquid metal sensor [21].

REFERENCES

[1] O. Yasa, Y. Toshimitsu, M. Y. Michelis, L. S. Jones, M. Filippi, T. Buchner, and R. K. Katzschmann, "An overview of soft robotics," *Annual Review of Control, Robotics, and Autonomous Systems*, vol. 6, no. 1, pp. 1–29, 2023.

[2] B. Jamil, N. Oh, J.-G. Lee, H. Lee, and H. Rodrigue, "A review and comparison of linear pneumatic artificial muscles," *International Journal of Precision Engineering and Manufacturing-Green Technology*, vol. 11, no. 1, pp. 277–289, 2024.

[3] R. Niiyama, X. Sun, C. Sung, B. An, D. Rus, and S. Kim, "Pouch motors: Printable soft actuators integrated with computational design," *Soft Robotics*, vol. 2, no. 2, pp. 59–70, 2015.

[4] D. Bruder and R. J. Wood, "The chain-link actuator: Exploiting the bending stiffness of mckibben artificial muscles to achieve larger contraction ratios," *IEEE Robotics and Automation Letters*, vol. 7, no. 1, pp. 542–548, 2022.

[5] J. Yi, X. Chen, C. Song, and Z. Wang, "Fiber-reinforced origamic robotic actuator," *Soft robotics*, vol. 5, no. 1, pp. 81–92, 2018.

[6] J. H. Jang, B. Jamil, Y. Moon, A. Coutinho, G. Park, and H. Rodrigue, "Design of gusseted pouch motors for improved soft pneumatic actuation," *IEEE/ASME Transactions on Mechatronics*, vol. 28, no. 6, pp. 3053–3063, 2023.

[7] N. Oh, Y. J. Park, S. Lee, H. Lee, and H. Rodrigue, "Design of paired pouch motors for robotic applications," *Advanced Materials Technologies*, vol. 4, no. 1, p. 1800414, 2019.

[8] C. T. O'Neill, C. M. McCann, C. J. Hohimer, K. Bertoldi, and C. J. Walsh, "Unfolding textile-based pneumatic actuators for wearable applications," *Soft Robotics*, vol. 9, no. 1, pp. 163–172, 2022.

[9] L. Ge, F. Chen, D. Wang, Y. Zhang, D. Han, T. Wang, and G. Gu, "Design, modeling, and evaluation of fabric-based pneumatic actuators for soft wearable assistive gloves," *Soft robotics*, vol. 7, no. 5, pp. 583–596, 2020.

[10] P. Arens, D. A. Quirk, W. Pan, Y. Yacoby, F. Doshi-Velez, and C. J. Walsh, "Preference-based assistance optimization for lifting and lowering with a soft back exosuit," *Science Advances*, vol. 11, no. 15, p. eadu2099, 2025.

[11] Y. M. Zhou, C. J. Hohimer, H. T. Young, C. M. McCann, D. Pont-Esteban, U. S. Civici, Y. Jin, P. Murphy, D. Wagner, T. Cole *et al.*, "A portable inflatable soft wearable robot to assist the shoulder during industrial work," *Science Robotics*, vol. 9, no. 91, p. eadi2377, 2024.

[12] J. Yang, M. Runciman, J. Avery, Z. Sun, and G. Mylonas, "A soft inflatable robot driven by hydraulic folded pouch actuators for minimally invasive surgery," *IEEE Robotics and Automation Letters*, vol. 9, no. 5, pp. 4870–4877, 2024.

[13] J. Yang, X. Li, M. Runciman, J. Avery, Z. Zhou, Z. Sun, and G. Mylonas, "A novel, soft, cable-driven parallel robot for minimally invasive surgeries based on folded pouch actuators," *Applied Sciences*, vol. 14, no. 10, p. 4095, 2024.

[14] P. Hyatt, D. Wingate, and M. D. Killpack, "Model reference predictive adaptive control for large-scale continuum robots," *Frontiers in Robotics and AI*, vol. 7, p. 558027, 2020.

[15] M. Runciman, J. Avery, M. Zhao, A. Darzi, and G. P. Mylonas, "Deployable, variable stiffness, cable driven robot for minimally invasive surgery," *Frontiers in Robotics and AI*, vol. 6, p. 141, 2020.

[16] D. E. Rumelhart, G. E. Hinton, and R. J. Williams, "Learning representations by back-propagating errors," *Nature*, vol. 323, no. 6088, pp. 533–536, 1986.

[17] L. Lindenroth, D. Stoyanov, K. Rhode, and H. Liu, "Toward intrinsic force sensing and control in parallel soft robots," *IEEE/ASME Transactions on Mechatronics*, vol. 28, no. 1, pp. 80–91, 2022.

[18] S. Hochreiter and J. Schmidhuber, "Long short-term memory," *Neural Computation*, vol. 9, no. 8, pp. 1735–1780, 1997.

[19] M. Hofer, C. Sferrazza, and R. D'Andrea, "A vision-based sensing approach for a spherical soft robotic arm," *Frontiers in Robotics and AI*, vol. 8, p. 630935, 2021.

[20] J. Avery, M. Runciman, A. Darzi, and G. P. Mylonas, "Shape sensing of variable stiffness soft robots using electrical impedance tomography," in *2019 international conference on robotics and automation (ICRA)*. IEEE, 2019, pp. 9066–9072.

[21] I. Adibnazari, B. J. Jeon, Y.-L. Park, and M. T. Tolley, "Versatile rotary actuators for small-scale robotic systems," in *2020 3rd IEEE International Conference on Soft Robotics (RoboSoft)*. IEEE, 2020, pp. 873–878.